Chemical and Biological Technologies in Agriculture

RESEARCH

Open Access

Reduced graphene oxide-based nanometal-composite containing copper and silver nanoparticles protect tomato and pepper against *Xanthomonas euvesicatoria* infection

Zuzana Bytešníková[1], Jakub Pečenka[3], Dorota Tekielska[3], Tomáš Kiss[3], Pavel Švec[1], Andrea Ridošková[1], Petr Bezdička[5], Jana Pekárková[2,6], Aleš Eichmeier[3], Robert Pokluda[4], Vojtěch Adam[1,2] and Lukáš Richtera[1,2*]

Abstract

Xanthomonas euvesicatoria (Xe) is of the genera *Xanthomonas*, which causes a bacterial spot disease that affects tomato and pepper plants, resulting in significant economic losses. Commonly used bactericides lead to pathogen resistance, environmental contamination and a current risk to human health. Herein, a nanocomposite consisting of Cu and Ag loaded onto reduced graphene oxide (rGO) was synthesized, characterized and tested. After confirmation of the antibacterial properties in vitro, nanocomposites at concentrations of 50 and 500 µg mL^{-1} were applied to protect tomato and pepper plants under controlled greenhouse conditions. The tomato and pepper plants indicated significantly lower disease severity when treated with the nanocomposite (15.6 and 16.7%, respectively) than when treated with the commercial copper-based bactericide Kocide® 2000. The nanocomposite was demonstrated as a high-efficiency biocide and has the potential for crop disease management with no phytotoxic effect.

Keywords: Graphene oxide, Copper, Silver, Nanoparticles, Bacterial spot disease, *Solanum lycopersicum*, *Capsicum* spp., Plants

*Correspondence: lukas.richtera@mendelu.cz

[1] Department of Chemistry and Biochemistry, Mendel University in Brno, Zemědělská 1, 613 00 Brno, Czech Republic
Full list of author information is available at the end of the article

Graphical Abstract

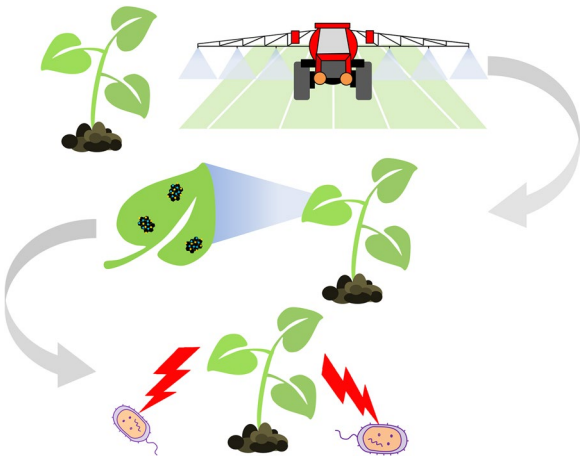

Introduction

In 2020 according to the Food and Agriculture Organization (FAO), the world production of tomato and pepper was approx. 187 million tons and 36 million tons, respectively. *Xanthomonas euvesicatoria (X. euvesicatoria*, Xe*)* is one of the causal agents of bacterial spot disease [1, 2]. This disease affects tomato (*Solanum lycopersicum* L.) and pepper (*Capsicum* spp.) all over the world, but especially in warm and humid areas, and manifests as lesions on leaves, fruits and stems [3]. Infected leaves show blight and necrosis and exhibit early leaf fall. This results in a decrease in photosynthesis and fruit damage, causing serious economic losses [4, 5]. The disease is commonly transmitted by rainwater from plant residues due to humid conditions [6, 7]. *Xanthomonas* spp. can persist as infectious for a long time and survive in plant residues or contaminated seeds as a latent infection [8]. The primary management strategy should include the use of certified seeds or disease-free transplant material, treating seeds with hot water and disposing of potential sources of infection, such as the physical removal of diseased crop material [9]. As a result of the resistance to streptomycin in *Xanthomonas* in the 1960s, copper-based bactericides combined with mancozeb or maneb (ethylene-bis-dithiocarbamates) have been used since that time [10, 11]. However, this solution has been indicated to be ineffective in the presence of copper-tolerant strains and in the case of weather conditions that are ideal for disease development [12]. Molecular additives [13] and antibiotics such as kasugamycin and streptomycin have been extensively tested, but resistance to these alternatives soon emerged [14–17]. Better results were obtained after combining antibiotics with copper [13]. The breeding of resistant cultivars is a possible option in the fight against bacterial spot disease. However, these resistant cultivars may be ineffective due to the shifting of bacterial populations that can occur before the resistant cultivars are deployed [18].

In recent decades, nanotechnologies have experienced well-deserved popularity due to their excellent qualities in different fields. In the agricultural sector, one of the most desirable applications of nanomaterials is disease management [19]. It is necessary to apply modern approaches in agriculture because compounds that are protective against plant pathogens should be efficient and at the same time should not be toxic to the environment or, more importantly, to humans. Although the possible risks associated with nanomaterials are not the subject of this study, they should not be underestimated. The agriculture sector is expected to see a drastic change in the coming era due to the large-scale applications of nanotechnology. As we know that "technology-yes, but safety-must", the possible risk associated with nano-fertilizers should also be considered before implementing these new technologies. Food and feed risk assessment after the exposition of nano-pesticides should be the subject of comprehensive studies for each type of studied nanomaterial separately [20, 21]. A wide spectrum of nanomaterials for plant disease control was recently studied including iron- [22, 23], carbon- [24], cobalt- [25], zinc- [26], silver- [27], or copper-based nanomaterials [28–30]. Silver nanoparticles (Ag NPs) are known for their excellent antibacterial properties against a wide range of microorganisms [31, 32] and are used in various fields, including food packaging [33], water treatment [34], dressing materials [35], and antibacterial agents [36].

Their disadvantage, which reduces their effectiveness, is their aggregation and oxidation [37]. Copper-containing biocides are attractive in agriculture due to their antibacterial effects and low cost. Copper nanoparticles (Cu NPs) have better antibacterial properties than copper salts due to their large surface area and resistance to being washed out during watering or rain [38, 39]. However, if Cu NPs are agglomerated, their effect decreases rapidly [40]. Graphene oxide (GO) is a unique material with excellent chemical and physical properties that has been used in many industries, environmental applications, biomedical equipment, and agriculture due to its biocompatibility and low cost [41–43]. In agriculture, GO has been used, for example, in the slow release of fertilizers and bactericides and the adsorption of heavy metals and toxins [44–47]. The nanocomposite synthesis consists of in situ formations of NPs onto GO with simultaneous reduction of GO resulting in a reduced GO (rGO). The rGO also exhibits biocompatibility and its field of application is similarly large as for GO [48–50].

In the present study, reduced graphene oxide (rGO) decorated with Cu and Ag NPs (rGO-Cu-Ag) was prepared, where rGO acted as a stabilizing agent to prevent the aggregation of Cu and Ag NPs and thereby improved the antibacterial properties of the NPs and facilitated the adherence of the nanocomposite to plant leaves. The synthesized rGO-Cu-Ag nanocomposite was applied to tomato and pepper leaves after its antibacterial activity was tested in vitro. In addition, the phytotoxicity of the prepared nanocomposite was tested. The effectiveness of the nanocomposite was compared with that of non-bonded NPs. In addition, changes in cell morphology after the application of the nanocomposite were studied.

Experimental section

Materials and chemicals

The chemicals used in this study, unless otherwise stated, were purchased from Sigma-Aldrich (St. Louis, MO, USA). The chemicals were analytical grade, and demineralized water was produced using an Aqual 25 reverse osmosis apparatus (Aqual, Česká, Czech Republic) and further treated with a Millipore System (Millipore System Inc., Billerica, MA, USA) to obtain ultrapure water with a corresponding resistivity of 18.20 MΩ cm (at 25 °C). All experiments used this ultrapure water unless otherwise stated. The pH values were evaluated using a pH meter (WTW inoLab, Weilheim, Germany) with a WTW SenTix pH electrode. For the determination of metals using atomic absorption spectroscopy, demineralized water obtained with a Millipore Milli-Q system (Millipore, Bedford, MA, USA) was used.

Synthesis on nanomaterials

Preparation of graphene oxide (GO)

GO was prepared by the chemical oxidation of 5.0 g graphite flakes (Sigma–Aldrich, 100 mesh, ≥ 75% min) in a mixture of concentrated H_2SO_4 (670 mL) and 30.0 g $KMnO_4$ according to the modified Hummer's method [51, 52]. The reaction mixture was stirred vigorously. After 10 days, the oxidation of graphite was terminated by the addition of H_2O_2 solution (250 mL, 30 wt% in H_2O, Penta, Prague, Czech Republic). The formed GO was washed 3 times with 1 M HCl (37 wt% in H_2O, Penta) and several times with ultrapure water (total volume used 60 L) until a constant pH value (3–4) was achieved.

Synthesis of the rGO-Cu-Ag nanocomposite

Solutions of $AgNO_3$ (25.0 mL, 10 mM) and $Cu(CH_3COO)_2$ (25.0 mL, 10 mM) were added dropwise to a solution of GO (1.0 mL, 5.0 mg mL^{-1}) under vigorous stirring. Then, the reducing agent $Na[BH_4]$ (40 mg) was slowly added to the reaction mixture, and the resulting mixture was stirred vigorously for 24 h at room temperature. The prepared nanocomposite was washed three times with 50.0 mL ultrapure water. The centrifuged nanocomposite (10 min, 6500 rcf) (Universal 320, Hettich, Tuttlingen, Germany) was filled up to a final volume 10.0 mL. Synthesis of rGO-Ag and rGO-Cu nanocomposites

For the synthesis of rGO-Ag, solutions of $AgNO_3$ (50.0 mL, 10 mM) were added dropwise to a solution of GO (1.0 mL, 5.0 mg mL^{-1}) under vigorous stirring. Then, the reducing agent $Na[BH_4]$ (40 mg) was slowly added to the reaction mixture, and the resulting mixture was stirred vigorously for 24 h at room temperature. The prepared nanocomposite was washed three times with 50.0 mL ultrapure water. The centrifuged nanocomposites (10 min, 6500 rcf) (Universal 320, Hettich, Tuttlingen, Germany) was filled up to a final volume 10.0 mL. The procedure for the synthesis of rGO-Cu was the same as that for rGO-Ag, and only $AgNO_3$ was replaced with $Cu(CH_3COO)_2$.

Characterization of the rGO-Cu-Ag nanocomposite

Scanning electron microscopy and energy-dispersive X-ray spectroscopy (EDS)

The morphologies of the samples were determined using scanning electron microscopy (SEM). The dispersed samples were diluted 1:20 with ultrapure water and then applied to silicon wafers from Siegert Wafer company (Siegert Wafer GmbH, Aachen, Germany) and allowed to dry at room temperature (20–25 °C). Images of the samples were obtained using a MAIA 3 SEM (TESCAN Ltd,

Brno, Czech Republic). An In-Beam SE detector with an accelerating voltage of 5 kV, a working distance of 3 mm and 50,000-fold magnification was used. Full frame capture was performed in UH Resolution mode and accumulation of image with image shift correction enabled, and it took approximately 0.5 min with the ~ 0,32 µs/pixel dwell time. The spot size was set at 2.4 nm.

To check the elemental compositions of the generated nanocomposites, energy-dispersive X-ray spectroscopy (EDS) analysis was performed using an EDX detector made on a MIRA 2 SEM (TESCAN Ltd, Brno, Czech Republic). An Everhart–Thornley scintillation detector was used with an accelerating voltage of 15 kV and a work distance of 15 mm. The power of the detector was set so that the input signal was approximately 19,000–21,000 cts. At this setting, the output signal was approximately 15,000–16,000 cts, and the detector dead-time fluctuated between 19 and 21%. The time for each analysis was 10 min. The spot size was 40 nm.

Transmission electron microscopy (TEM) analysis and EDS

The samples were studied by an FEI Talos F200X HRTEM operated at 200 kV with a maximum beam current of 1.0 nA. The lower amount of beam current was chosen so as not to damage the GO in the samples. The microscope was equipped with a Super-X EDS system with four silicon drift detectors (SDDs) enabling element mapping. The samples were prepared on Au grid coated with a holey carbon film.

Determination of the Cu and Ag concentrations in rGO-Cu-Ag by atomic absorption spectrometry (AAS)

For the atomic absorption spectrometry (AAS) analysis, 0.1 mL of rGO-Cu-Ag, rGO-Ag, and rGO-Cu samples were decomposed with reaction mixtures containing 5.0 mL of suprapure HNO_3 (70%, Merck, Germany) and 5.0 mL of Milli-Q water at 210 °C for 35 min (15 min operating temperature, 20 min holding time) using an Ethos ONE microwave extractor (Milestone, Sorisole, Italy). Determination of the Cu and Ag contents in the samples was performed using a 240 FS AA atomic absorption spectrometer (Agilent Technologies, Santa Clara, CA, USA) with flame atomization acetylene–air flame (oxygen flow 13.5 L min^{-1} and acetylene 2.0 L min^{-1}). Standard solutions of Cu and Ag (1000 mg L^{-1}, Merck, Darmstadt, Germany) were used to prepare the calibration solutions, which were acidified with 1 wt% concentrated suprapure HNO_3. All solutions were prepared using demineralized water obtained with a Millipore Milli-Q system (Millipore, Bedford, MA, USA). The wavelength for Cu was 324.8 nm and for Ag was 328.1 nm.

Attenuated total reflectance Fourier transform infrared spectroscopy (ATR FTIR)

Fourier transform infrared spectroscopy (FTIR) spectra were collected using an INVENIO R FTIR spectrometer equipped with a single-reflection diamond ATR accessory—A225/Q Platinum ATR module (Bruker Optic Inc., Billerica, MA, USA). A fixed load was applied to each small amount of sample to ensure full contact of the solid with the diamond surface. Solid samples were directly analysed in lyophilized form. Before each measurement, background spectra were collected. Spectra were recorded at 25 °C from 4000 to 400 cm^{-1} at a resolution of 2 cm^{-1}. Each spectrum was acquired by merging 128 interferograms. Bruker OPUS 8.1 (Bruker Optic Inc., Billerica, MA, USA) software was used for the spectra recording, and JDXview v0.2 software written by Norbert Haider, Vienna, Austria was used for further spectral evaluation [53].

X-ray powder diffraction (XRPD) sample preparation

A thin layer of a corresponding sample was deposited on the surface of a Si zero-background sample holder by evaporating water from the suspension. All the as-prepared samples on a zero-background sample holder were then placed into the sample holders for XRPD analysis.

X-ray powder diffraction–conventional Bragg–Brentano reflection geometry

Diffraction patterns were collected with a PANalytical X'Pert PRO diffractometer (Malvern Panalytical, Malvern, Worcestershire, United Kingdom) equipped with a conventional X-ray tube (Cu Kα radiation, 40 kV, 30 mA) and a linear position sensitive detector PIXcel with an anti-scatter shield. A programmable divergence slit set to a fixed value of 0.25°, Soller slit of 0.04 rad and mask of 15 mm were used in the primary beam. A programmable anti-scatter slit set to a fixed value of 0.25°, a Soller slit of 0.04 rad and a Ni beta-filter were used for the diffracted beam. Data were collected in the range of 5–90° 2θ with a step of 0.0131° and 500 s per step, producing a scan of approximately 3 h 46 min.

Evaluation of X-ray patterns

Qualitative analysis was performed with the HighScorePlus software package (Malvern PANalytical, The Netherlands, version 5.1.0) together with the PDF-4 + database [54]. Line profile analysis was performed using routines implemented in the HighScorePlus software [55]. Diffraction lines were fitted using the Pseudo Voigt profile function with split width and shape. No background subtraction was performed. The calculated values of the integral breadths of the diffraction lines (B_{obs}) were then

corrected for instrumental broadening (B_{std}). The net values of the integral breadths (B_{struct}) and the positions of the diffraction lines were then entered into the Scherrer formula [56] to obtain the appropriate crystallite size in the corresponding direction. K (crystal shape factor) corresponding to the cubic shape of particles ($K=1$) was used. The correction for instrumental broadening was performed with the NIST SRM660a standard (LaB_6) that was analysed with the same geometry, and the B_{std} values were determined by the same procedure.

Raman spectroscopy

A Renishaw InVia Raman microscope (Gloucestershire, UK) was used to collect the Raman spectra. A laser beam with a wavelength of 633 nm was used to excite the molecules, and 0.75 mW of laser energy (5% of 15 mW) was used. The sample surfaces were investigated via a 50 × L objective. The time per spectrum was 5 s, and 32 repeats of spectra were collected and further analysed in Renishaw WiRE software version 5.2. When the spectra repeats were averaged and smoothed, the bands were identified after subtracting the baselines.

Atomic force microscopy (AFM)

A Bruker Dimension FastScan atomic force microscope (Bruker Nano Surface, Santa Barbara, CA, USA) operated in PeakForce tapping mode was used for GO and rGO-Cu-Ag characterization. Silicon nitride triangular cantilevers "SCANASYST-AIR" (Bruker Nano Surface) characterized by a spring constant of 0.671 N m^{-1} and a sensitivity of 91.67 nm V^{-1} equipped with a tetrahedral silicon tip with a nominal tip radius of 2 nm were used for imaging. Images were taken at 1000 × 1000 pixels with a PeakForce Tapping frequency of 2 kHz and an amplitude of 55 nm. The gain parameters were set automatically by the ScanAsyst algorithm. All images were collected under ambient conditions at 38% relative humidity and 22.5 °C with a scanning raster rate of 0.67 Hz.

X-ray photoelectron spectroscopy (XPS)

X-ray photoelectron spectroscopy (XPS, Kratos Axis Supra with monochromatic Al Kα X-ray radiation, emission current of 15 mA and hybrid lens mode, Manchester, UK) was used for the analysis of the surface of the rGO-Cu-Ag nanocomposite. High-resolution spectra were measured with a pass energy of 20 eV. The spectra were fitted using a combination of Gaussian–Lorentzian line shapes in CasaXPS software version 2.3.22. The Shirley algorithm was used to establish the background of the spectra.

Antibacterial testing

Antibacterial assay, minimum inhibitory concentration (MIC) and minimum bactericidal concentration (MBC)

The antibacterial activity of the rGO-Cu-Ag nanocomposite against *X. euvesicatoria* was evaluated by the determination of viable bacteria using the colony-forming unit (CFU) enumeration technique. Preliminary determination of MIC was carried out as an evaluation of the individual nanocomposites at final concentrations of 0.01, 0.1, and 5 μg mL^{-1}. The effectiveness of the rGO-Cu-Ag nanocomposite was compared with those of the single-metal nanocomposites containing reduced graphene oxide with copper (rGO-Cu) or silver (rGO-Ag). For this purpose, *X. euvesicatoria* strain no. 2968 obtained from the National Collection of Plant Pathogenic Bacteria (NCPPB, London, UK) was cultured in Luria–Bertani (LB) broth (Sigma-Aldrich) at 28 °C overnight. The obtained bacterial suspension was adjusted to an optical density of 0.1 at 600 nm (OD600) (approx. 1×10^8 CFU mL^{-1}) and then serially diluted in LB broth to a concentration of approx. 2×10^6 CFU mL^{-1}. The nanocomposites were mixed with bacterial suspension and incubated for 24 h at 28 °C with continuous shaking at 110 rpm (ES–20, Biosan, Warren, Michigan, USA). For the nontreated control, ultrapure water was used instead of the nanocomposites. To determine the number of viable bacteria, the pour plate method was used. In detail, 100 μL samples from each mixture were diluted in a decimal series of 10^{-5}–10^{-6}. A volume 100 μL from each dilution was pipetted on the centre of a sterile Petri dish (90 mm diameter). Sterile, molten (44 to 46 °C) plate count agar (Himedia, Mumbai, India) was added and mixed with the sample by swirling the plate. The samples were cooled at room temperature until solidified and then inverted and incubated at 28 °C until bacterial colonies were visible on nontreated control plates. Subsequently, bacterial colonies formed in or on the plate were counted. The effect on bacterial growth was reported as a percent of the CFU number for the nontreated control. A similar assay was used to determine the minimum bactericidal concentration (MBC) of the rGO-Cu-Ag nanocomposite. The nanocomposite was used at concentrations of 6.25, 12.5, 25.0 and 50.0 μg mL^{-1}. The MIC value was established by the lowest concentration of rGO-Cu-Ag nanocomposite that did not permit any visible growth of *X. euvesicatoria* in or on the plate count medium. This was done by observing post-incubated agar plates for the presence or absence of bacteria after 72 h.

Observation of morphological changes in bacteria

Fresh bacterial cultures were prepared in LB broth for 24 h at 28 °C. The bacterial suspension was diluted with sterile saline containing the nanocomposite and shaken at 120 rpm overnight. The final concentration of the nanocomposite in the solution was 0, 6.25, 12.5, 25.0, 50.0 and 500 μg mL^{-1}. The solution was centrifuged at 7000 g for 15 min, and the pellet was washed 3 times in 10 mL of ultrapure water. For the evaluation of bacterial cell morphology in the presence of the tested nanocomposite, the washed pellet was dispersed in 2 mL of ultrapure water and diluted 100 times. Then, 5 μL of suspension was loaded on a silicon wafer and allowed to dry in laminar flow. Images of the samples were made using a SEM, MAIA 3, Brno, Czech Republic. The detector was an external SE detector with an accelerating voltage of 2 kV, and the work distance was 3 mm and was scanned by using analytical mode.

DNA analysis

The bacterial suspension was prepared as described above, mixed with fresh LB broth to OD600 = 0.1 corresponding to 1×10^8 CFU and cultivated overnight with the nanocomposite at concentrations of 6.25, 12.5, 25.0 and 50.0 μg mL^{-1}. Sterile saline was used as a positive control instead of the nanocomposite. Samples were centrifuged in 2-mL tubes at 15,000 g for 5 min, and total DNA was extracted from the pellet using Nucleospin Tissue (Macherey Nagel, Düren, Germany) according to the manufacturer's protocol. DNA samples were mixed with 5X Green GoTaq Reaction Buffer (Promega, Madison, WI, USA) and run on a 1.2% agarose gel (Thermo Fisher Scientific, Waltham, MA, USA) coloured by GelRed (Biotium, Fremont, CA, USA). Samples were visualized using a UV transilluminator MUV21—312 (Major Science, Saratoga, California, USA).

Plant testing

Greenhouse experiment

Cultivars of pepper cv. Citrina and tomato cv. Mandat were used as plant material. Plants were grown in 280 mL pots containing standard substrate TS 4 (Klasmann-Deilmann GmbH, Geeste, Germany) and kept in greenhouse conditions at 22–26 °C and ≥ 70% relative humidity. For the experiment, plants at the four-leaf stage were used. According to the antibacterial assay, the rGO-Cu-Ag concentration of 50 μg mL^{-1} was selected as potentially effective for the plant treatment. To test the phytotoxicity of the nanocomposites on the plants, a concentration of 500 μg mL^{-1} was also included. The nanocomposites were applied to the plants by spraying (LaboPlast Spray Bottle, nozzle diameter 0.6 mm, Bürkle GmbH, Ban Bellingen, Germany), and after 24 h, the plants were sprayed using a 1×10^8 CFU bacterial suspension. After inoculation, the plants were covered by polyethylene bags for 48 h to increase the humidity. In the positive control, sterile saline was used instead of the nanocomposite. Plants in the negative control were sprayed with nanocomposites at a concentration of 500 μg mL^{-1}, and sterile saline was used instead of bacteria. Negative control samples were used to evaluate the phytotoxicity of rGO-Cu-Ag. As another plant treatment, a 0.35% solution of the commercial product Kocide® 2000 (DuPont, Wilmington, DE, USA) was applied according to the manufacturer's protocol. The experiment was carried out in two repetitions. In total, eight plants per treatment were used. The evaluation of disease symptoms was carried out on the seventh and fourteenth days after inoculation. The occurrence of bacterial spots was evaluated using a four-point scale: 0—healthy leaves without symptoms, 1—low symptom occurrence (1–3 dots per leaf), 2—1/3 of the leaf surface infected, 3—high symptom occurrence (more than 1/3 of the leaf surface infected). Based on symptom evaluation, the disease severity (DS) was calculated using the following formula [57]:

$$DS(\%) = \frac{\sum \left(number\ of\ plants\ in\ a\ disease\ scale\ point \times disease\ scale\ point \right)}{\left(total\ number\ of\ plants \times maximum\ disease\ scale\ point \right)} \times 100.$$

Relative quantification of gene expression

Samples of tomato plants treated with 500 μg mL^{-1} rGO-Cu-Ag and inoculated with *X. euvesicatoria* (rGO-Cu-Ag + Xe), treated with 500 μg mL^{-1} rGO-Cu-Ag and noninoculated (rGO-Cu-Ag), nontreated and inoculated with *X. euvesicatoria*, and nontreated and noninoculated (NTC) were used for gene expression analysis. For each sample, four leaves of one plant were harvested 21 days after treatment. Plant samples were frozen at − 80 °C and ground to a fine powder using a mortar and pestle. An amount 100 mg of homogenized tissue were used for total RNA extraction using Spectrum Plant total RNA (Sigma-Aldrich, St. Louis, MO, USA) according to the manufacturer's instructions. Extracted RNA was quantified by a Modulus™ Single Tube Multimode Reader (Turner BioSystems, Sunnyvale, CA, USA) using a Quant-iT™ RiboGreen™ RNA Assay Kit (Invitrogen, Carlsbad, CA, USA), and the concentrations of all samples were adjusted to 75 ng μL^{-1}. Reverse transcription was performed using random hexamer primers (Roche,

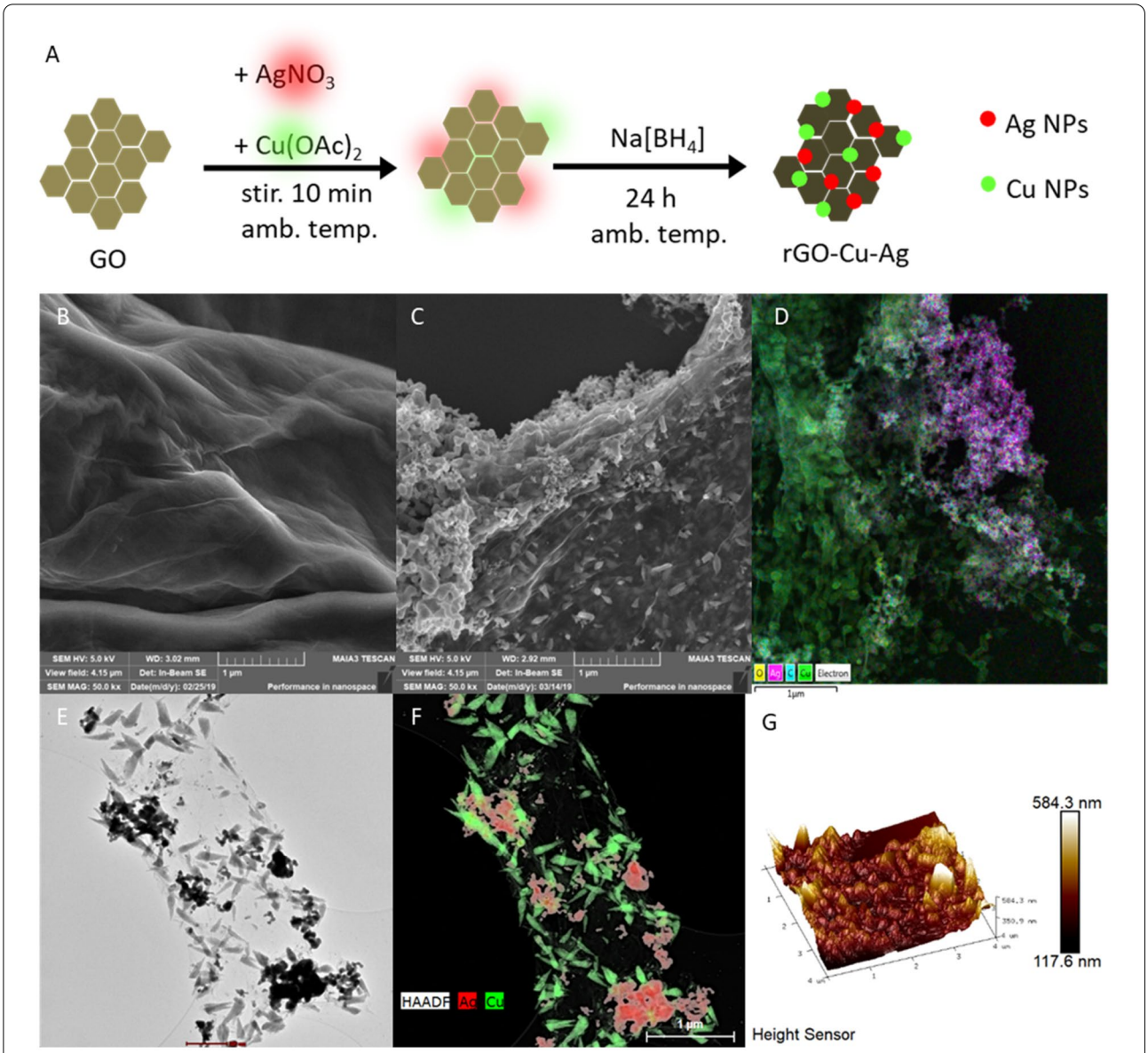

Fig. 1 Schematic illustration of the synthesis procedure of the rGO-Cu-Ag nanocomposite (**A**), scanning electron microscopy (SEM) images of the starting material GO (**B**), prepared nanocomposite rGO-Cu-Ag (**C**), and energy-dispersive X-ray spectroscopy (EDS) image of rGO-Cu-Ag showing elemental composition (**D**), transmission electron microscopy (TEM) image of rGO-Cu-Ag (**E**) and conformation of the presence of copper and silver (**B**) from high-angle annular dark-field imaging (HAADF), atomic force microscopy (AFM) 3D image of the rGO-Cu-Ag nanocomposite visualized by height sensor (G)

Basel, Switzerland) and RevertAid Reverse Transcriptase (Thermo Fisher Scientific, Waltham, MA, USA). The cDNA was used as a template for the real-time PCR with the primer pairs and is shown in Additional file 1: Table. S1.

Betatubulin was used as a reference gene for the normalization of gene expression between the samples. The real-time PCR of a 20 µL volume consisted of 1 × Hot-Sybr qPCR Kit (MCLab, San Francisco, CA, USA), 2 µL of prepared cDNA, 0.3 µM of each primer of the primer pair, and PCR grade water. The reactions for each sample were prepared in duplicate and run using a real-time PCR cycler RotorGene 3000 (Corbett Research, Sydney, Australia). The cycling conditions were 10 min at 95 °C, 40 cycles of 1 min at 95 °C, 1 min at 58 °C, and 1 min at 72 °C for Btub [58], PR1 [59], CAT [60] and TomQ'a [61]. The temperature profile for the qPCR of the PoP [62] and PRQb [61] genes was 10 min at 95 °C, 40 cycles

of 15 s at 95 °C, 1 min at 60 °C, and 1 min at 72 °C. For relative quantification, the Livak and Schmittgen [63] method was used, and the analyses were performed using qbase + software (Biogazelle, Zwijnaarde, Belgium).

Statistical analysis

The obtained data were analysed by Statistica CZ software (StatSoft, Prague, Czech Republic). The data were subjected to analysis by single-factor ANOVA. Statistical differences ($\alpha = 0.05$) were determined according to Duncan's test. Gene expression data were subjected to analysis by the single-factor ANOVA test ($p < 0.05$), and the differences between the variants were then determined according to Tukey's test using qbase + software (Biogazelle, Gent, Belgium).

Results and discussion

Characterization of the rGO-Cu-Ag nanocomposite

The synthesis of the rGO-Cu-Ag nanocomposite, which is illustrated in detail in Fig. 1A, started with the synthesis of GO from graphite flakes by a modified Hummer's method. The microstructure of GO was confirmed by SEM, as shown in Fig. 1B. The GO sheets were large and smooth with fine wrinkles. The morphology and topography of GO were also studied using AFM, and fine single-layer material was observed, which was used for the synthesis of the nanocomposite (Additional file 1: Fig. S1). Cu and Ag NPs were immobilized on the GO surface using $Na[BH_4]$ as a reducing agent. The resulting material was a rGO-Cu-Ag nanocomposite with uniformly distributed NPs on the surface. Although Ag NPs and Cu NPs do not have any modification on their surface preventing their aggregation, since they are still bound onto GO, GO prevents their aggregation. The morphology of the rGO-Cu-Ag nanocomposite was observed using SEM (Fig. 1C). The EDS micrograph (Fig. 1D) of rGO-Cu-Ag confirmed the elemental composition, including the presence of copper, silver, carbon and oxygen. The morphologies of rGO-Ag and rGO-Cu as control materials are shown in Additional file 1: Fig. S2, and their elemental mappings are shown in Additional file 1: Fig. S3. Both materials exhibited complete coverage of rGO with nanoparticles that were equally distributed on the surface of rGO. The TEM image in Fig. 1E confirms the equal distribution of the copper and silver NPs onto rGO, which is confirmed with elemental mapping (Fig. 1F) using high-angle annular dark-field imaging (HAADF). The copper NPs have a rugby ball shape, while the silver NPs have a spherical shape, which is typical for silver NPs. Figure 1G shows the structure of the rGO-Cu-Ag nanocomposite in 3D views for better observation of the morphology and topography of the material. AAS was used for the quantification of the single-metal content in the nanocomposites. The concentrations of metals in nanocomposite rGO-Cu-Ag were 1466 mg L^{-1} and 2312 mg L^{-1} for copper and silver, respectively. The concentration of silver in rGO-Ag was 6154 mg L^{-1} and the concentration of copper in rGO-Cu was 2231 mg L^{-1}.

FTIR analysis was used to confirm the structure of the prepared rGO-Cu-Ag nanocomposite by detecting the changes in the functional groups of GO and rGO-Cu-Ag (Additional file 1: Fig. S4). GO shows a large number of functional groups compared to rGO-Cu-Ag, which corresponds to a high degree of oxidation and thus the presence of functional groups. Conversely, the elimination of these groups in rGO-Cu-Ag suggests a successful reduction [64]. The spectrum of GO shows the presence of bands associated with C–O (1050 cm^{-1}), C=C (1631 cm^{-1}), C=O (1737 cm^{-1}), and C–H (2925 cm^{-1}). The broad peak at 3322 cm^{-1} corresponds to O–H vibrations [64–66]. The rGO-Cu-Ag spectrum exhibits peaks corresponding to C–O (1105 cm^{-1} and 1339 cm^{-1}) and O–H (2998 cm^{-1} and 3549 cm^{-1}). After reduction by $Na[BH_4]$, the O–H groups are retained, and additional hydroxyls are introduced as a result of the hydrolysis of boron esters [66]. XPS analysis was performed to determine the surface composition of the rGO-Cu-Ag nanocomposite. Characteristic XPS spectra for rGO-Cu-Ag nanocomposites in the C 1 s, Ag 3d and Cu 2p regions are presented in Fig. 2A, B, C, respectively. The high-resolution spectrum of rGO-Cu-Ag shows three peaks in the C 1 s region: carbon sp^2 at 284.81 eV, C–OH at 286.61 eV and C–O–C at 288.1 eV (Fig. 1A) [67]. A small Si–C peak at 282.48 eV is also observed, which corresponds to the silicon wafer substrate in sample preparation for XPS analysis [68]. The higher intensity of the sp^2 carbon peak compared to the C–OH, C=O and O=C–O peaks confirms the reduction of GO [69]. The Ag 3d XPS (Fig. 2B) spectrum exhibits Ag $3d_{5/2}$ and Ag $3d_{3/2}$ peaks at 368.49 and 374.54 eV binding energies with a 6 eV difference, indicating metallic Ag in the hybrid nanocomposite, which is indicative of Ag^0 on the surface of the rGO sheets and confirms the oxidation state of Ag^0 [70]. The high values of the Ag peaks indicate the interaction of Ag with rGO and CuO. The Cu 2p spectrum of the sample is presented in Fig. 2C. The two peaks centred at binding energies of 932.76 and 953.04 eV are attributed to the Cu $2p_{3/2}$ and Cu $2p_{1/2}$ of CuO, respectively. Moreover, the shake-up satellite peaks of Cu $2p_{3/2}$ and Cu $2p_{1/2}$ at 940.71 and 960.99 eV, respectively, confirms the formation of CuO. A small peak at 935.54 eV corresponds to $Cu(OH)_2$ [71]. The results are in accordance with those of XRD. Furthermore, we analysed GO and rGO-Cu-Ag by Raman spectroscopy. The D and G Raman bands were detected at 1323 cm^{-1} and 1582 cm^{-1} for GO and 1307 cm^{-1} and 1590 cm^{-1} for rGO-Cu-Ag. The Raman

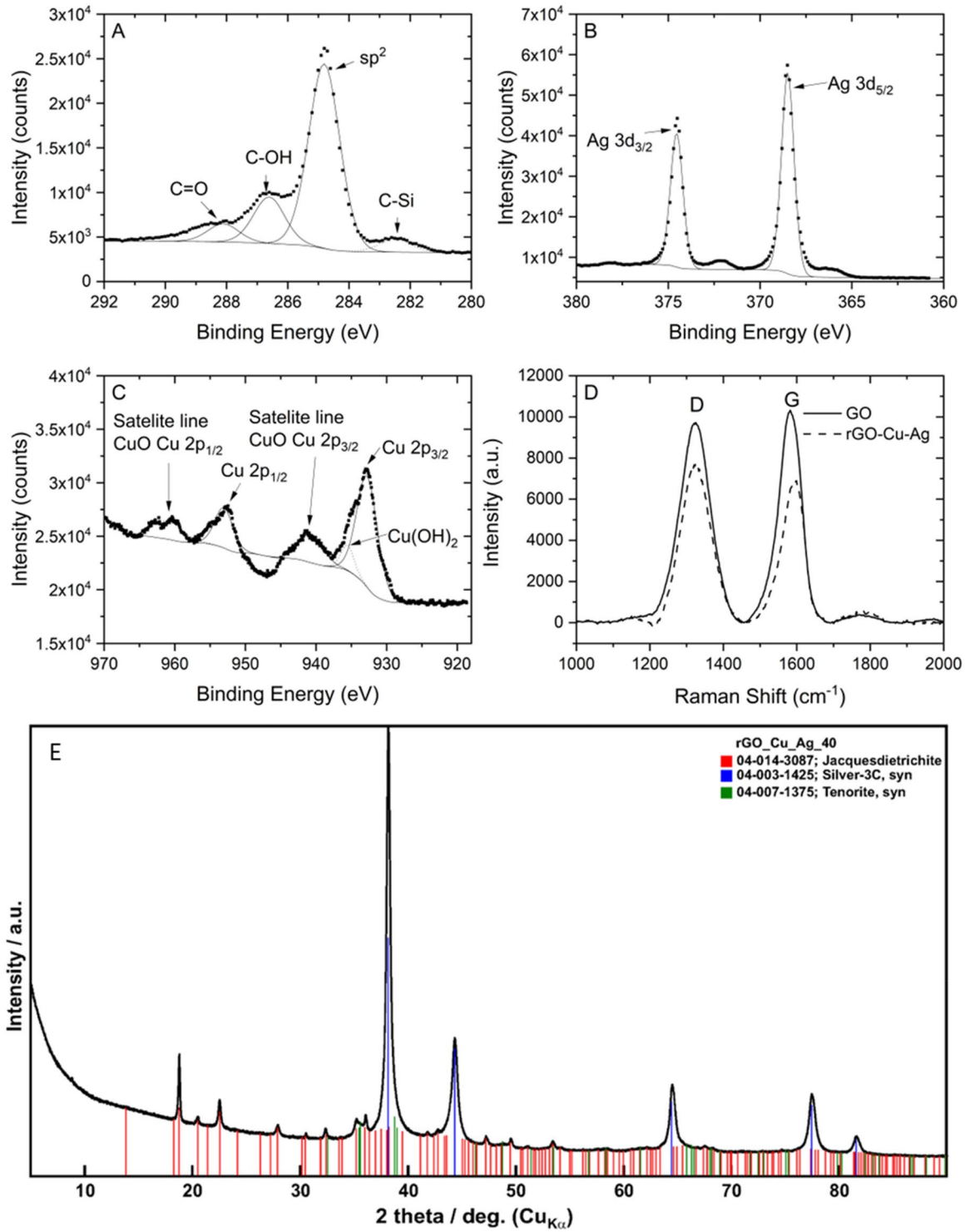

Fig. 2 XPS analysis of rGO-Cu-Ag for C 1 s (**A**) Ag 3d (**B**) Cu 2p (**C**), Raman spectra of GO and the rGO-Cu-Ag nanocomposite (**D**), and X-ray powder diffraction of rGO-Cu-Ag (**E**)

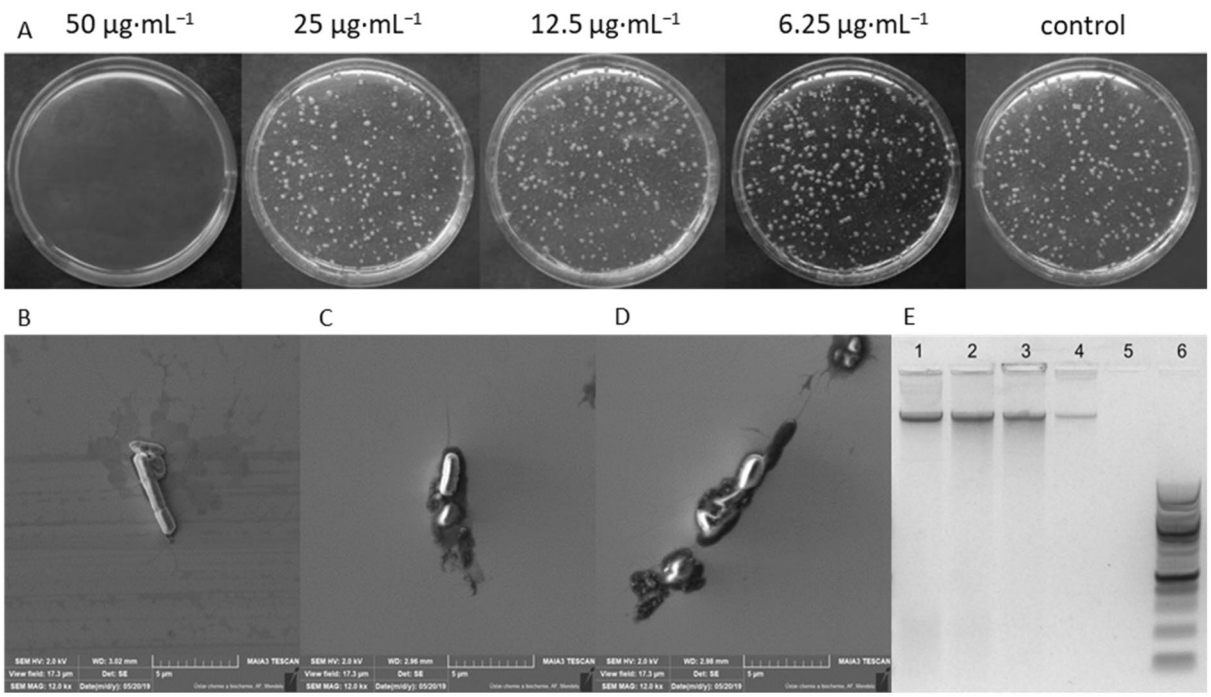

Fig. 3 Minimum bactericidal concentration (MBC) of the rGO-Cu-Ag composite. Growth of *X. euvesicatoria* treated with different rGO-Cu-Ag concentrations (shown above each plate) in comparison with the nontreated control (**A**). SEM images of *X. euvesicatoria* cells untreated (**B**) and treated with 50 µg mL^{-1} (**C**) and 500 µg·mL^{-1} rGO-Cu-Ag (**D**). Samples of total DNA extracted from the *X. euvesicatoria* NCPPB 2968 samples after cultivation with different concentrations of the rGO-Cu-Ag nanocomposite. The positive control sample without nanocomposite treatment is represented by lane 1. Lanes 2 to 5 represent nanocomposite concentrations of 6.25, 12.5, 25.0 and 50.0 µg mL^{-1}, respectively. Lane 6 represents 100 kb ladder (**E**)

intensity ratio of the D and G bands (I_D/I_G) increased in the case of rGO-Cu-Ag (0.99) compared to GO (0.94) (Fig. 2D), which is in accordance with the literature [72, 73]. Figure 2E shows the XRD patterns of rGO-Cu-Ag. A characteristic GO peak is missing, confirming the successful reduction of GO [74]. In addition to the confirmation of the presence of silver in the form of nanoparticles, copper was present in two forms. The first form was expectedly CuO as a mineral tenorite, whose chemical formula is CuO [75], and the second was basic copper (II) dihydroxoborate (PDF-4+# 04-014-3087) [76], which was probably formed due to the sodium borohydride that was used as a reducing agent.

Antibacterial activity of rGO-Cu-Ag nanocomposite

Antibacterial activity, MICs and MBCs of nanocomposites

The antibacterial properties of the rGO-Cu-Ag nanocomposite against the *X. euvesicatoria* strain were investigated in vitro in comparison to copper (rGO-Cu) and silver nanoparticles (rGO-Ag). As shown in Additional file 1: Table. S2, bacterial growth was inhibited, and the MICs of all three tested nanomaterials were determined at a concentration of 5 µg mL^{-1}. The strong inhibition in the case of rGO-Ag could be explained by the high content of silver, which was approx. 2.7 times higher than that of rGO-Cu-Ag. Despite the higher copper content (approx. 1.5 times higher than that of rGO-Cu-Ag), no significant effect was observed for rGO-Cu at concentrations of 0.1 and 0.01 µg mL^{-1}. On the other hand, the rGO-Cu-Ag concentrations of 0.1 and 0.01 µg mL^{-1} significantly reduced bacterial growth, probably due to the synergistic effect of copper and silver. Our results correspond to those of studies, in which the antibacterial activities of nanocomposites containing GO and nanoparticles were presented [19, 77, 78]. Moreover, the increased antimicrobial activity of silver and copper due to the synergistic effect [79–83] was also described. Based on these results, the MBC of rGO-Cu-Ag was determined. However, only a concentration of 50 µg mL^{-1} entirely inhibited bacterial growth 72 h after incubation (Fig. 3A). The results of the in vitro antibacterial assay provided the basis for the selection of two concentrations of the rGO-Cu-Ag nanocomposite for the further treatment of plants in the greenhouse experiment.

Nanocomposite influence on bacterial DNA content

Copper and silver nanoparticles are well known for their antibacterial effects. Both Cu NPs and Ag NPs penetrate cells, causing cell death [84, 85]. Cu NPs are known to bind and interact with cellular DNA. Intercellular Cu NPs affect DNA replication and break DNA structures [78]. Ag NPs have also been widely presented as substances that can be incorporated into the cell membrane, leading to the disruption of cell metabolism. The influence of our rGO-Cu-Ag nanocomposite containing both types of NPs should lead to the decreased replication of bacterial cells and total DNA. Figure 3E represents the total DNA extracted from the *X. euvesicatoria* cells cultivated with rGO-Cu-Ag. A strong band of high molecular weight DNA observed belonging to the positive control sample where the nanocomposite was replaced by sterile saline (lane 1). This result was equal to that of the sample of containing 6.25 and 12.5 μg mL^{-1} rGO-Cu-Ag (lanes 2 and 3). A significant reduction in DNA content was observed at concentrations of 25 μg mL^{-1} rGO-Cu-Ag; (lane 4). The strongest effect was observed in the sample with the highest nanocomposite concentration with no visible band of DNA (lane 5, 50 μg mL^{-1} rGO-Cu-Ag). This corresponds to inhibition of *X. euvesicatoria* cell growth in the case of 50 μg mL^{-1} rGO-Cu-Ag (Fig. 3A). Moreover, the reduction in DNA content corresponds to cell growth inhibition as well as to the decomposing DNA already present in the samples (lanes 4 and 5), confirming the ability of our nanocomposite to penetrate bacterial cells.

Analysis of morphological changes in cells

The morphological bacterial cell changes were observed by SEM. The untreated bacterial cells (Fig. 3B) remained intact with no significant changes. Nevertheless, bacterial cells after incubation with both tested concentrations (Fig. 3C, D) showed ruptured cell membranes, released cellular contents and cell death. The antibacterial activity of rGO has been attributed to the stress of the membrane induced by the sharp edges of the rGO sheets, which could result in mechanical damage to the cell membrane, leading to the loss of bacterial membrane/wall integrity and the leakage of bacterial content [86]. Cu NPs have a positive charge, which could attract them to negatively charged bacterial cell surfaces to react with sulfur- and phosphorous-containing compounds [87, 88]. Ag NPs release Ag^{+} ions that bind to the thiol groups in proteins and enzymes on the bacterial wall and induce cell wall damage [89, 90].

Plant protection

To examine its antibacterial effect and ability to suppress bacterial spot disease, the nanocomposite was applied to tomato and pepper plants inoculated with *X. euvesicatoria*. The nanocomposite was applied at concentration 50 μg mL^{-1}, which was selected based on the in vitro antibacterial assay. Moreover, we applied also the concentration 500 μg mL^{-1} as well as a 0.35% solution of Kocide® 2000 to see the effects (i) on plant and (ii) on bacteria. Plants were evaluated for the occurrence of bacterial spot symptoms on the 7th and 14th days after inoculation. The disease severity was assessed using a four-point scale (Fig. 4A–H and I–P), and the disease severity index was calculated for each variant. The results obtained for the tomato (Fig. 4Q) and pepper (Fig. 4R) plants at 7 days after inoculation indicated significantly lower disease severity when treated with rGO-Cu-Ag (15.6 and 16.7%, respectively) than when treated with Kocide® 2000 (34.4 and 38.5%, respectively) and from the positive control (77.1 and 71.9%, respectively). Observations performed on the 14th day after inoculation showed a slight increase in symptom severity in comparison to the evaluation on the 7th day, proportionally for each variant. Moreover, both tomato and pepper plants exhibited significantly reduced symptoms when treated with a concentration of 500 μg mL^{-1} compared with 50 μg mL^{-1}. This indicates that the minimum bactericidal concentration obtained during the in vitro test was not effective at the same level after application to plants. On the other hand, the copper content in rGO-Cu-Ag was only ~ 146.6 and ~ 14.7 μg mL^{-1} at concentrations of

(See figure on next page.)

Fig. 4 Representation of the scale used for symptoms of black spot evaluation in the greenhouse experiment on pepper plants. 0—healthy leaves without symptoms (**A**–**B**), 1—low occurrence of symptoms (**C**–**D**), 2—1/3 of the leaf surface infected (**E**–**F**), 3—high symptoms occurrence (more than 1/3 of the leaf surface infected) (**G**–**H**). Representation of the scale used for symptoms of black spot evaluation in the greenhouse experiment on tomato plants. 0—healthy leaves without symptoms (**I**–**J**), 1—low occurrence of symptoms (**K**–**L**), 2—1/3 of the leaf surface infected (**M**–**N**), 3—high symptoms occurrence (more than 1/3 of the leaf surface infected) (**O**–**P**). Severity of black spot disease symptoms on tomato (**Q**) and pepper (**R**) plants. Statistical differences were proven for all means of disease severity on both the 7th and 14th days after inoculation (DAI) (Duncan's test, $p \leq 0.05$). The error bar represents the standard error of the mean. Gene expression in tomato plants (S) (PR1-pathogenesis-related protein 1; polyphenol oxidase precursor; CAT-catalase, PRQb- class III basic β-1,3-glucanase, class III acidic β-1,3-glucanase-TomQ'a). Different letters above the bars indicate statistically significant differences among treatments (single-factor ANOVA, $p < 0.05$; Tukey's test, $p < 0.05$)

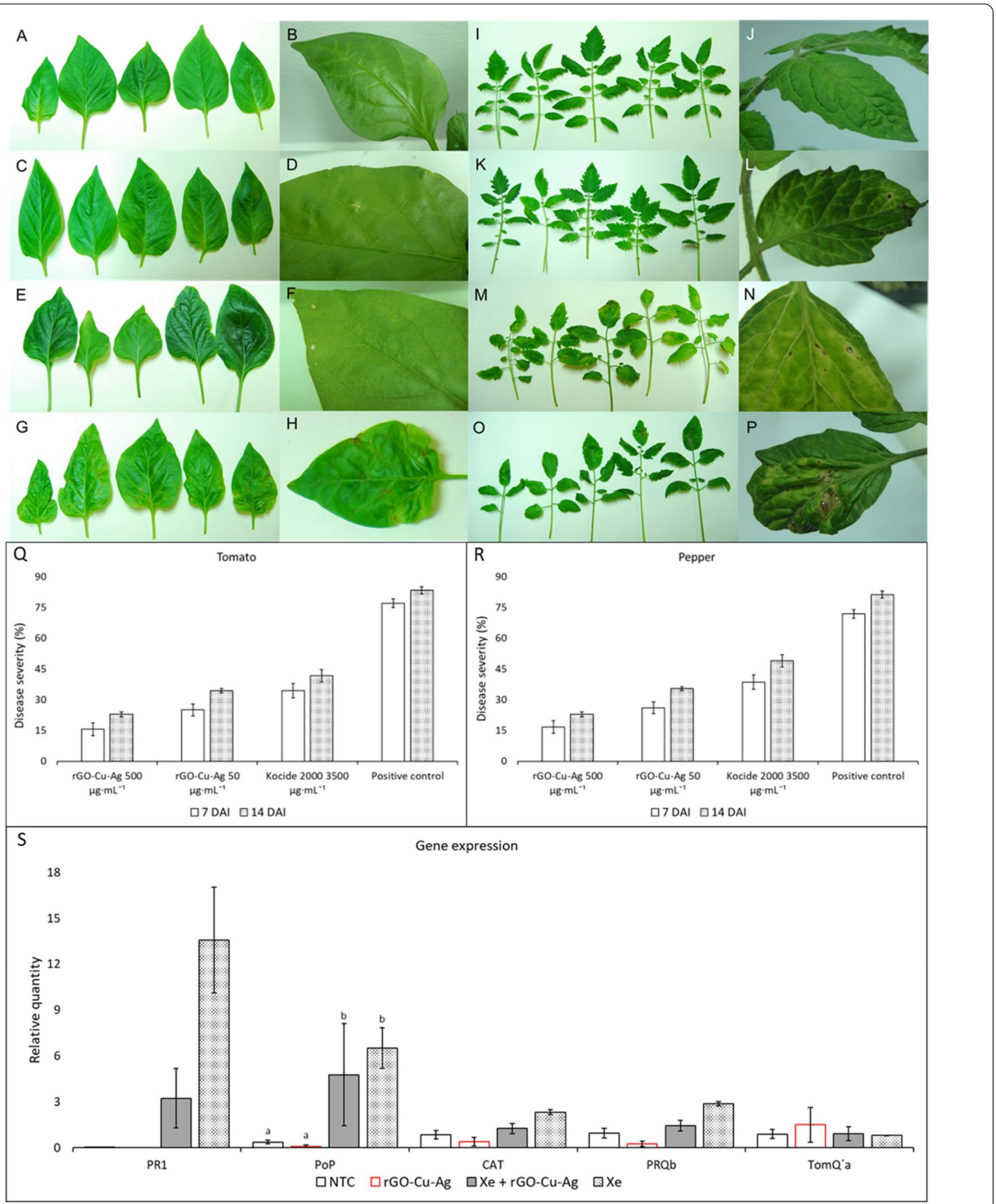

Fig. 4 (See legend on previous page.)

500 µg mL^{-1} and 50 µg mL^{-1}, respectively, in comparison with the 0.35% Kocide® 2000 solution, the copper content of which was ~ 1226.5 µg mL^{-1}.

To examine the phytotoxicity, a negative control was included in the greenhouse experiment. Plants were sprayed with the nanocomposite at concentrations of

50 and 500 μg mL^{-1} [26, 29, 91], and sterile saline was used instead of bacterial inoculum. The plants were then monitored for the occurrence of any rGO-Cu-Ag toxicity symptoms. Throughout the duration of the experiment, we observed no visible negative influence of the nanocomposite on plant growth and development; therefore, we conclude that the concentration of 500 μg mL^{-1} was not toxic to the tested plants. No inhibitory effects of plant growth by the used concentrations were observed. Comprehensive review by Zhang et al. [92] describes more positive than negative effects of graphenoxide composites on plant growth in general. There is mainly positive effect on tomato plants growth as increase the root fresh weight [93] or accelerated seed germination and promotion of shoot and root elongation [94].

Gene expression analysis

Genes for the five proteins that are involved in plant defence mechanisms were selected for gene expression analysis (Fig. 4S): pathogenesis-related protein 1 (PR1), catalase (CAT), class III basic β-1,3-glucanase (PRQb) class III acidic β-1,3-glucanase (TomQ'a) and polyphenol oxidase precursor (PoP). β-1,3-Glucanases are hydrolytic enzymes that are part of defence genes induced by pathogen infection in higher plants. Moreover, catalase (CAT) is related to the production of reactive oxygen species (ROS) and, together with glucans (PRQb), is involved in the response to metal stress [95]. According to the results, the treatment with the nanocomposite did not affect the expression of either gene involved in metal stress (CAT and PRQb), with expression levels similar to those of the nontreated variants. Thus, the treatment does not induce stress to plants via this pathway. This is in accordance with Noori et al. [96], where the lower toxicity of CuNPs/AgNPs is mentioned in comparison with that of sources of free Cu/Ag ions such as $CuCl_2$ or $AgNO_3$. Treatment with nanocomposites alone also did not affect the expression of genes involved in the response to pathogen infection, and for the PR1 gene coding pathogenesis-related protein 1, no detectable expression was observed in the plants treated only with nanocomposites. On the other hand, in the inoculated plants, the nanocomposite treatment reduced the expression of some pathogen response genes (PR1 and PoP), showing a decrease in plant response activity to pathogen infection. Here, the highest difference was observed for the PR1; however, the difference between the variants was not significant. Significant differences were observed only for the PoP protein, where the noninoculated tomato plants had significantly reduced expression compared to the inoculated ones. While the phytotoxicity of the CuNPs/AgNPs is, however, often mentioned [97–99], no negative effect of our nanocomposite was observed for the tomato plants. Nevertheless, the entrapment of our CuNPs and AgNPs on rGO probably did not lead to phytotoxicity, while the desired antibacterial activity remained in effect. These results are similar to those of studies demonstrating a favourable effect of complexes containing CuNPs [100–102] or AgNPs [103, 104] on tomato growth, quality or health.

Conclusion

Copper and silver NPs were successfully loaded onto rGO by a facile reduction method. The remarkable antibacterial activity of rGO-Cu-Ag against *X. euvesicatoria* was demonstrated at a relatively low concentration (50 μg mL^{-1}). In addition, the nanocomposite antibacterial properties were enhanced compared to the corresponding single-metal composites rGO-Cu and rGO-Ag, which confirmed the synergistic effect of the silver and copper NPs bonded onto rGO. rGO-Cu-Ag significantly reduced the bacterial spot severity of tomato and pepper plants in greenhouse conditions with a substantially lower content of copper, which was at least 8.3 times higher in the case of the commercial preparation. Moreover, no phytotoxic effect was observed even at a concentration ten times higher than the minimum bactericidal concentration. Furthermore, the results from SEM and DNA content analyses indicated that the nanocomposite can disrupt bacterial cell integrity and inhibit the replication of bacteria. Further studies should be performed to clarify the antibacterial mechanisms of the nanocomposite. Nevertheless, the results in this work could promote the future use of rGO-Cu-Ag as a powerful antibacterial agent with potential applications in agriculture.

Supplementary Information

The online version contains supplementary material available at https://doi.org/10.1186/s40538-022-00347-7.

Additional file 1: Fig S1. AFM image of GO. **Fig S2.** SEM image of rGO-Ag (A) and rGO-Cu (B) nanocomposites. **Fig S3.** Elemental mapping confirming the presence of the silver in the rGO-Ag (A) and copper in the rGO-Cu (B). **Fig S4.** FTIR spectra of GO and rGO-Cu-Ag nanocomposite. **Table S1.** cDNAs used for real-time PCR. **Table S2.** Antibacterial effect of nanomaterials on *X. euvesicatoria* growth. Results based on colony forming unit enumeration shown as the bacterial growth in percent from nontreated control which was 100%.

Acknowledgements

This work was financially supported by ERDF 'Multidisciplinary research to increase application potential of nanomaterials in agricultural practice' (No. CZ.02.1.01/0.0/0.0/16_025/0007314). The authors acknowledge the assistance provided by the Research Infrastructure NanoEnviCz, supported by the Ministry of Education, Youth and Sports of the Czech Republic under Project No. LM2018124. We would also like to thank Moravoseed CZ a.s. We acknowledge CF Nanobiotechnology of CIISB, Instruct-CZ Centre, supported by MEYS CR (LM2018127). We also acknowledge CzechNanoLab Research Infrastructure supported by MEYS CR (LM2018110).

Author contributions
ZB: conceptualization, methodology, writing—original draft, investigation; JP: methodology, writing—original draft, investigation; DT: formal analysis, data curation; TK: formal analysis, data curation; PS: formal analysis, data curation; AR: formal analysis, data curation; JP: visualization, data curation; PB: visualization, formal analysis, data curation. A.E.: writing—review and editing; R.P.: writing—review and editing ; V.A.: supervision, writing—review and editing; L.R.: supervision, writing—review and editing. All authors read and approved the final manuscript.

Funding
European Regional Development Fund, CZ.02.1.01/0.0/0.0/16_025/0007314. Ministry of Education, Youth and Sport of the Czech Republic, LM2018124. Ministry of Education, Youth and Sport of the Czech Republic, LM2018127. Ministry of Education, Youth and Sport of the Czech Republic, LM2018110.

Declarations

Ethics approval and consent to participate
Not applicable.

Consent for publication
Not applicable.

Competing interests
The authors declare that they have no competing interests.

Author details
[1]Department of Chemistry and Biochemistry, Mendel University in Brno, Zemědělská 1, 613 00 Brno, Czech Republic. [2]Central European Institute of Technology, Brno University of Technology, Purkyňova 656/123, 612 00 Brno, Czech Republic. [3]Mendeleum - Institute of Genetics, Faculty of Horticulture, Mendel University in Brno, Valtická 334, 69144 Lednice, Czech Republic. [4]Department of Vegetable Growing and Floriculture, Faculty of Horticulture, Mendel University in Brno, Valtická 337, 691 44 Lednice, Czech Republic. [5]Institute of Inorganic Chemistry of the Czech Academy of Sciences, Husinec-Řež 1001, 250 68, Husinec-Řež, Czech Republic. [6]Department of Microelectronics, Faculty of Electrical Engineering and Communication, Brno University of Technology, Technická 3058/10, 616 00 Brno, Czech Republic.

Received: 15 September 2022 Accepted: 20 October 2022
Published online: 14 November 2022

References

1. Moretti C, Amatulli MT, Buonaurio R. PCR-based assay for the detection of *Xanthomonas euvesicatoria* causing pepper and tomato bacterial spot. Lett Appl Microbiol. 2009;49(4):466–71.
2. Giovanardi D, et al. Impact of bacterial spot outbreaks on the phytosanitary quality of tomato and pepper seeds. Plant Pathol. 2018;67(5):1168–76.
3. Jones JB, et al. Reclassification of the *xanthomonads* associated with bacterial spot disease of tomato and pepper. Syst Appl Microbiol. 2004;27(6):755–62.
4. Stall RE, et al. 2 Genetically diverse groups of strains are included in *Xanthomonas-campestris pv vesicatoria*. Int J Syst Bacteriol. 1994;44(1):47–53.
5. Obradovic A, et al. Characterization and PCR-based typing of *Xanthomonas campestris pv. vesicatoria* from peppers and tomatoes in serbia. Eur J Plant Pathol. 2004;110(3):285–92.
6. Araujo ER, et al. Widespread distribution of *Xanthomonas perforans* and limited presence of X. gardneri in Brazil. Plant Pathol. 2017;66(1):159–68.
7. Mcinnes TB, et al. Airborne dispersal of bacteria in tomato and pepper transplant fields. Plant Dis. 1988;72(7):575–9.
8. Mcguire RG, Jones JB, Scott JW. Epiphytic populations of *Xanthomonas-campestris pv vesicatoria* on tomato cultigens resistant and susceptible to bacterial spot. Plant Dis. 1991;75(6):606–9.
9. Janse JD, Wenneker M. Possibilities of avoidance and control of bacterial plant diseases when using pathogen-tested (certified) or -treated planting material. Plant Pathol. 2002;51(5):523–36.
10. Marco GM, Stall RE. Control of bacterial spot of pepper initiated by strains of *Xanthomonas-campestris pv-vesicatoria* that differ in sensitivity to copper. Plant Dis. 1983;67(7):779–81.
11. Conover RA, Gerhold NR. Mixtures of copper and maneb or mancozeb for control of bacterial spot of tomato and their compatibility for control of fungus diseases. Proc Fla State Hortic Soc. 1981;94:154–6.
12. Obradovic A, et al. Management of tomato bacterial spot in the field by foliar applications of bacteriophages and SAR inducers. Plant Dis. 2004;88(7):736–40.
13. Worthington RJ, et al. Foliar-applied small molecule that suppresses biofilm formation and enhances control of copper-resistant *Xanthomonas euvesicatoria* on pepper. Plant Dis. 2012;96(11):1638–44.
14. Vallad GE, et al. Comparison of Kasugamycin to traditional bactericides for the management of bacterial spot on tomato. Horts. 2010;45(12):1834–40.
15. Minsavage GV, Canteros BI, Stall RE. plasmid-mediated resistance to streptomycin in *Xanthomonas-Campestris* pv vesicatoria. Phytopathology. 1990;80(8):719–23.
16. Lai M, Shaffer S, Panopoulos NJ. Stability of plasmid-borne antibiotic-resistance in *Xanthomonas-Vesicatoria* in infected tomato leaves. Phytopathology. 1977;67(12):1527–30.
17. Thayer PL, Stall RE. Effect of variation in bacterial spot pathogen of pepper and tomato on control with streptomycin. Phytopathology. 1961;51(8):568.
18. Gassmann W, et al. Molecular evolution of virulence in natural field strains of *Xanthomonas campestris* pv. vesicatoria. J Bacteriol. 2000;182(24):7053–9.
19. Ocsoy I, et al. Nanotechnology in plant disease management: dna-directed silver nanoparticles on graphene oxide as an antibacterial against *Xanthomonas perforans*. ACS Nano. 2013;7(10):8972–80.
20. Acharya A, Pal PK. Agriculture nanotechnology: translating research outcome to field applications by influencing environmental sustainability. Nanoimpact. 2020;19:100232.
21. Wang DJ, et al. Nano-enabled pesticides for sustainable agriculture and global food security. Nat Nanotechnol. 2022;17(4):347–60.
22. Elbasuney S, et al. Ferric oxide colloid: towards green nano-fertilizer for tomato plant with enhanced vegetative growth and immune response against fusarium wilt disease. J Inorg Organometallic Polym Mat. 2022. https://doi.org/10.1007/s10904-022-02442-6.
23. Ahmed T, et al. Bioengineered chitosan-iron nanocomposite controls bacterial leaf blight disease by modulating plant defense response and nutritional status of rice (*Oryza sativa L.*). Nano Today. 2022;45:101547.
24. Luo X, et al. Nitrogen-doped carbon dots alleviate the damage from tomato bacterial wilt syndrome: systemic acquired resistance activation and reactive oxygen species scavenging. Environ Sci-Nano. 2021;8(12):3806–19.
25. Hoang AS, et al. Evaluation of metal nano-particles as growth promoters and fungi inhibitors for cereal crops. Chem Biol Technol Agric. 2022;9:1.
26. Zhao WC, et al. Engineered Zn-based nano-pesticides as an opportunity for treatment of phytopathogens in agriculture. Nanoimpact. 2022;28:100420.
27. Ha STT, et al. Regulation of botrytis cinerea infection and gene expression in cut roses by using nano silver and salicylic acid. Plants-Basel. 2021;10:6.
28. Attia MS, et al. Protective role of copper oxide-streptomycin nano-drug against potato brown rot disease caused by *Ralstonia solanacearum*. J Cluster Sci. 2022;33(4):1373–86.
29. Elmer WH, et al. Foliar application of copper oxide nanoparticles suppresses fusarium wilt development on chrysanthemum. Environ Sci Technol. 2021;55(15):10805–10.
30. Shang HP, et al. Copper oxide nanoparticle-embedded hydrogels enhance nutrient supply and growth of lettuce (*Lactuca sativa*) infected with fusarium oxysporum f sp lactucae. Environ Sci Technol. 2021;55(20):13432–42.
31. Zheng KY, et al. Antimicrobial cluster bombs: silver nanoclusters packed with daptomycin. ACS Nano. 2016;10(8):7934–42.

32. Datta LP, et al. Enzyme responsive nucleotide functionalized silver nanoparticles with effective antimicrobial and anticancer activity. New J Chem. 2017;41(4):1538–48.
33. Tavakoli H, et al. The effect of nano-silver packaging in increasing the shelf life of nuts: An in vitro model. Ital J Food Safety. 2017;6(4):156–61.
34. Lv YH, et al. Silver nanoparticle-decorated porous ceramic composite for water treatment. J Membr Sci. 2009;331(1–2):50–6.
35. Rujitanaroj PO, Pimpha N, Supaphol P. Wound-dressing materials with antibacterial activity from electrospun gelatin fiber mats containing silver nanoparticles. Polymer. 2008;49(21):4723–32.
36. Chernousova S, Epple M. Silver as antibacterial agent: ion, nanoparticle, and metal. Angew Chem Int Ed. 2013;52(6):1636–53.
37. Huang JF, et al. Facile pyrolysis preparation of rosin-derived biochar for supporting silver nanoparticles with antibacterial activity. Compos Sci Technol. 2017;145:89–95.
38. Bogdanovic U, et al. Copper nanoparticles with high antimicrobial activity. Mater Lett. 2014;128:75–8.
39. Young M, Santra S. Copper (Cu)-silica nanocomposite containing valence-engineered cu: a new strategy for improving the antimicrobial efficacy of cu biocides. J Agric Food Chem. 2014;62(26):6043–52.
40. Karlsson HL, et al. Copper oxide nanoparticles are highly toxic: a comparison between metal oxide nanoparticles and carbon nanotubes. Chem Res Toxicol. 2008;21(9):1726–32.
41. Chen JN, et al. Graphene oxide exhibits broad-spectrum antimicrobial activity against bacterial phytopathogens and fungal conidia by intertwining and membrane perturbation. Nanoscale. 2014;6(3):1879–89.
42. Chabot V, et al. A review of graphene and graphene oxide sponge: material synthesis and applications to energy and the environment. Energy Environ Sci. 2014;7(5):1564–96.
43. Liu W, et al. Graphene enhances cellular proliferation through activating the epidermal growth factor receptor. J Agric Food Chem. 2016;64(29):5909–18.
44. Kim F, Cote LJ, Huang JX. Graphene oxide: surface activity and two-dimensional assembly. Adv Mater. 2010;22(17):1954–8.
45. Zhao GX, et al. Few-layered graphene oxide nanosheets as superior sorbents for heavy metal ion pollution management. Environ Sci Technol. 2011;45(24):10454–62.
46. Zhang M, et al. Slow-release fertilizer encapsulated by graphene oxide films. Chem Eng J. 2014;255:107–13.
47. Zhang LL, Jiang CL, Zhang ZP. Graphene oxide embedded sandwich nanostructures for enhanced Raman readout and their applications in pesticide monitoring. Nanoscale. 2013;5(9):3773–9.
48. Gurunathan S, et al. Biocompatibility of microbially reduced graphene oxide in primary mouse embryonic fibroblast cells. Colloids Surf B-Biointerfaces. 2013;105:58–66.
49. Kim YK, Kim MH, Min DH. Biocompatible reduced graphene oxide prepared by using dextran as a multifunctional reducing agent. Chem Commun. 2011;47(11):3195–7.
50. Narayanan KB, Kim HD, Han SS. Biocompatibility and hemocompatibility of hydrothermally derived reduced it graphene oxide using soluble starch as a reducing agent. Colloids Surf B-Biointerfaces. 2020. https://doi.org/10.1016/j.colsurfb.2019.110579.
51. Hummers WS, Offeman RE. Preparation of graphitic oxide. J Am Chem Soc. 1958;80(6):1339–1339.
52. Gao W, et al. New insights into the structure and reduction of graphite oxide. Nat Chem. 2009;1(5):403–8.
53. Haider, N. *JDXview*. 2005 https://homepage.univie.ac.at/norbert.haider/cheminf/jdxview.html.
54. Gates-Rector S, Blanton T. The powder diffraction file: a quality materials characterization database. Powder Diffr. 2019;34(4):352–60.
55. Degen T, et al. The highscore suite. Powder Diffr. 2014;29(S2):S13–8.
56. Scherrer P. Estimation of the size and internal structure of colloidal particles by means of röntgen. Nachr Ges Wiss Göttingen. 1918;2:96–100.
57. Jorge V, et al. QTL analysis of field resistance to *Xanthomonas axonopodis* pv. manihotis in cassava. Theor Appl Genet. 2001;102(4):564–71.
58. Lovdal T, Lillo C. Reference gene selection for quantitative real-time PCR normalization in tomato subjected to nitrogen, cold, and light stress. Anal Biochem. 2009;387(2):238–42.
59. Uehara T, et al. Resistant and susceptible responses in tomato to cyst nematode are differentially regulated by salicylic acid. Plant Cell Physiol. 2010;51(9):1524–36.
60. Zhang ZP, Miao MM, Wang CL. Effects of ALA on photosynthesis, antioxidant enzyme activity, and gene expression, and regulation of proline accumulation in tomato seedlings under NaCl stress. J Plant Growth Regul. 2015;34(3):637–50.
61. Ishihara T, et al. Transcriptome analysis of quantitative resistance-specific response upon ralstonia solanacearum infection in tomato. PLoS ONE. 2012;7:10.
62. Parker J, et al. Quantitative proteomics of tomato defense against *Pseudomonas syringae* infection. Proteomics. 2013;13(12–13):1934–46.
63. Livak KJ, Schmittgen TD. Analysis of relative gene expression data using real-time quantitative PCR and the 2− ΔΔCT method. Methods. 2001;25(4):402–8.
64. Ossonon BD, Belanger D. Synthesis and characterization of sulfophenyl-functionalized reduced graphene oxide sheets. RSC Adv. 2017;7(44):27224–34.
65. Lomeda JR, et al. Diazonium functionalization of surfactant-wrapped chemically converted graphene sheets. J Am Chem Soc. 2008;130(48):16201–6.
66. Dreyer DR, et al. The chemistry of graphene oxide. Chem Soc Rev. 2010;39(1):228–40.
67. Silva Filho JC, et al. A thermal method for obtention of 2 to 3 reduced graphene oxide layers from graphene oxide. SN Appl Sci. 2020;2:8.
68. Shimoda K, et al. Influence of surface structure of SiC nano-sized powder analyzed by X-ray photoelectron spectroscopy on basic powder characteristics. Appl Surf Sci. 2007;253(24):9450–6.
69. Kumara M, et al. Yolk type asymmetric Ag-Cu2O hybrid nanoparticles on graphene substrate as efficient electrode material for hybrid supercapacitors. J Res Phys Chem. 2019;233(1):85–104.
70. Shaikh A, Parida S, Boehm S. One step eco-friendly synthesis of Ag-reduced graphene oxide nanocomposite by phytoreduction for sensitive nitrite determination. RSC Adv. 2016;6(102):100383–91.
71. Akhavan O, et al. CuO/Cu(OH)(2) hierarchical nanostructures as bactericidal photocatalysts. J Mater Chem. 2011;21(26):9634–40.
72. Stankovich S, et al. Synthesis of graphene-based nanosheets via chemical reduction of exfoliated graphite oxide. Carbon. 2007;45(7):1558–65.
73. Krishnamoorthy K, et al. Investigation of raman and photoluminescence studies of reduced graphene oxide sheets. Appl Phys A. 2012;106(3):501–6.
74. Yasin G, et al. Exploring the nickel-graphene nanocomposite coatings for superior corrosion resistance: manipulating the effect of deposition current density on its morphology, mechanical properties, and erosion-corrosion performance. Adv Engin Mat. 2018;20:7.
75. Neto ME, et al. 2020 Early development of corn seedlings primed with synthetic tenorite nanofertilizer. Journal of Seed Science. 42
76. Vorobyova A, et al. One-dimensional magnet basic copper (ii) dihydroxoborate Cu 2 {BO (OH) 2}(OH) 3: synthesis and properties. Russ Chem Bull. 2020;69(4):704–11.
77. Liang Y, Yang DS, Cui JH. A graphene oxide/silver nanoparticle composite as a novel agricultural antibacterial agent against *Xanthomonas oryzae* pv. oryzae for crop disease management. J Chem. 2017;41(22):13692–9.
78. Li YD, Yang DS, J.H. Cui, Graphene oxide loaded with copper oxide nanoparticles as an antibacterial agent against *Pseudomonas syringae* pv. tomato. Rsc Adv. 2017;7(62):38853–60.
79. Lin YSE, et al. Individual and combined effects of copper and silver ions on inactivation of *Legionella pneumophila*. Water Res. 1996;30(8):1905–13.
80. Huang HI, et al. In vitro efficacy of copper and silver ions in eradicating *pseudomonas aeruginosa, Stenotrophomonas maltophilia and Acinetobacter baumannii*: implications for on-site disinfection for hospital infection control. Water Res. 2008;42(1–2):73–80.
81. Kuthati Y, et al. Phototherapeutic spectrum expansion through synergistic effect of mesoporous silica trio-nanohybrids against antibiotic-resistant gram-negative bacterium. J Photochem Photobiol B-Biol. 2017;169:124–33.
82. Targhi AA, et al. Synergistic effect of curcumin-Cu and curcumin-Ag nanoparticle loaded niosome: enhanced antibacterial and anti-biofilm activities. Bioorg Chem. 2021. https://doi.org/10.1016/j.bioorg.2021.105116.

83. Ashok B, et al. 2022 Nanocomposite cotton gauze cloth with in situ generated silver, copper and their binary metal nanoparticles by bioreduction method. Inorganic and Nano-Metal Chemistry.
84. Usman MS, et al. Synthesis, characterization, and antimicrobial properties of copper nanoparticles. Int J Nanomed. 2013;8:4467–78.
85. Rai M, Yadav A, Gade A. Silver nanoparticles as a new generation of antimicrobials. Biotechnol Adv. 2009;27(1):76–83.
86. Akhavan O, Ghaderi E. Toxicity of graphene and graphene oxide nanowalls against bacteria. ACS Nano. 2010;4(10):5731–6.
87. Raffi M, et al. Investigations into the antibacterial behavior of copper nanoparticles against *Escherichia* coli. Ann Microbiol. 2010;60(1):75–80.
88. Stoimenov PK, et al. Metal oxide nanoparticles as bactericidal agents. Langmuir. 2002;18(17):6679–86.
89. Duran N, et al. Potential use of silver nanoparticles on pathogenic bacteria, their toxicity and possible mechanisms of action. J Braz Chem Soc. 2010;21(6):949–59.
90. Marambio-Jones C, Hoek EMV. A review of the antibacterial effects of silver nanomaterials and potential implications for human health and the environment. J Nanopart Res. 2010;12(5):1531–51.
91. Tabatabaee S, et al. Copper nanoparticles mediated physiological changes and transcriptional variations in microRNA159 (miR159) and mevalonate kinase (MVK) in pepper; potential benefits and phytotoxicity assessment. J Environ Chem Engin. 2021;9:5.
92. Zhang X, et al. The effects of graphene-family nanomaterials on plant growth: a review. Nanomaterials. 2022;12:6.
93. Guo XH, et al. Effects of graphene oxide on tomato growth in different stages. Plant Physiol Biochem. 2021;162:447–55.
94. Zhang M, et al. Effects of graphene on seed germination and seedling growth. J Nanopart Res. 2015;17:2.
95. Zavaliev R, et al. Biology of callose (beta-1,3-glucan) turnover at plasmodesmata. Protoplasma. 2011;248(1):117–30.
96. Noori A, et al. Exposure of tomato (*Lycopersicon esculentum*) to silver nanoparticles and silver nitrate: physiological and molecular response. Int J Phytorem. 2020;22(1):40–51.
97. Tripathi DK, et al. Nitric oxide alleviates silver nanoparticles (AgNps)-induced phytotoxicity in pisum sativum seedlings. Plant Physiol Biochem. 2017;110:167–77.
98. Mehrian SK, et al. Effect of chemical synthesis silver nanoparticles on germination indices and seedlings growth in seven varieties of lycopersicon esculentum mill (tomato) plants. J Cluster Sci. 2016;27(1):327–40.
99. Ruttkay-Nedecky B, et al. Nanoparticles based on essential metals and their phytotoxicity. J Nanobiotechnol. 2017. https://doi.org/10.1186/s12951-017-0268-3.
100. Juarez-Maldonado A, et al. Cu Nanoparticles absorbed on chitosan hydrogels positively alter morphological, production, and quality characteristics of tomato. J Appl Botany Food Qual. 2016;89:183–9.
101. Hernandez HH, et al. Cu Nanoparticles in chitosan-PVA hydrogels as promoters of growth, productivity and fruit quality in tomato. Emir J Food Agri. 2017;29(8):573–80.
102. Lopez-Vargas ER, et al. Foliar application of copper nanoparticles increases the fruit quality and the content of bioactive compounds in tomatoes. Appl Sci-Basel. 2018;8:7.
103. Mahawar H, et al. Synergistic effects of silver nanoparticles augmented calothrix elenkinii for enhanced biocontrol efficacy against alternaria blight challenged tomato plants. 3 Biotech. 2020;10(3):1–10.
104. Santiago TR, et al. Green synthesis of silver nanoparticles using tomato leaf extract and their entrapment in chitosan nanoparticles to control bacterial wilt. J Sci Food Agric. 2019;99(9):4248–59.

Publisher's Note